

# Liver motion during cone beam computed tomography guided stereotactic body radiation therapy

Justin C. Park

*Center for Advanced Radiotherapy Technologies and Department of Radiation Medicine and Applied Sciences, University of California San Diego, La Jolla, California 92093 and Department of Electrical and Computer Engineering, University of California San Diego, La Jolla, California 92093*

Sung Ho Park,<sup>a)</sup> Jong Hoon Kim, Sang Min Yoon, and Si Yeol Song

*Department of Radiation Oncology, Asan Medical Center, College of Medicine, University of Ulsan, Seoul 138-736, South Korea*

Zhaowei Liu

*Department of Electrical and Computer Engineering, University of California San Diego, La Jolla, California 92093*

Bongyong Song, Kevin Kaweloa, Matthew J. Webster, Ajay Sandhu, Loren K. Mell, Steve B. Jiang, and Arno J. Mundt

*Center for Advanced Radiotherapy Technologies and Department of Radiation Medicine and Applied Sciences, University of California San Diego, La Jolla, California 92093*

William Y. Song<sup>b)</sup>

*Center for Advanced Radiotherapy Technologies and Department of Radiation Medicine and Applied Sciences, University of California San Diego, La Jolla, California 92093*

(Received 19 March 2012; revised 7 September 2012; accepted for publication 10 September 2012; published 2 October 2012)

**Purpose:** Understanding motion characteristics of liver such as, interfractional and intrafractional motion variability, difference in motion within different locations in the organ, and their complex relationship with the breathing cycles are particularly important for image-guided liver SBRT. The purpose of this study was to investigate such motion characteristics based on fiducial markers tracked with the x-ray projections of the CBCT scans, taken immediately prior to the treatments.

**Methods:** Twenty liver SBRT patients were analyzed. Each patient had three fiducial markers ( $2 \times 5$ -mm gold) percutaneously implanted around the gross tumor. The prescription ranged from 2 to 8 fractions per patient. The CBCT projections data for each fraction ( $\sim 650$  projections/scan), for each patient, were analyzed and the 2D positions of the markers were extracted using an in-house algorithm. In total,  $>55\,000$  x-ray projections were analyzed from 85 CBCT scans. From the 2D extracted positions, a 3D motion trajectory of the markers was constructed, from each CBCT scans, resulting in left-right (LR), anterior-posterior (AP), and cranio-caudal (CC) location information of the markers with  $>55\,000$  data points. The authors then analyzed the interfraction and intrafraction liver motion variability, within different locations in the organ, and as a function of the breathing cycle. The authors also compared the motion characteristics against the planning 4DCT and the RPM<sup>TM</sup> (Varian Medical Systems, Palo Alto, CA) breathing traces. Variations in the appropriate gating window (defined as the percent of the maximum range at which 50% of the marker positions are contained), between fractions were calculated as well.

**Results:** The range of motion for the 20 patients were  $3.0 \pm 2.0$  mm,  $5.1 \pm 3.1$  mm, and  $17.9 \pm 5.1$  mm in the planning 4DCT, and  $2.8 \pm 1.6$  mm,  $5.3 \pm 3.1$  mm, and  $16.5 \pm 5.7$  mm in the treatment CBCT, for LR, AP, and CC directions, respectively. The range of respiratory period was  $3.9 \pm 0.7$  and  $4.2 \pm 0.8$  s during the 4DCT simulation and the CBCT scans, respectively. The authors found that breathing-induced AP and CC motions are highly correlated. That is, all markers moved cranially also moved posteriorly and vice versa, irrespective of the location. The LR motion had a more variable relationship with the AP/CC motions, and appeared random with respect to the location. That is, when the markers moved toward cranial-posterior direction, 58% of the markers moved to the patient-right, 22% of the markers moved to the patient-left, and 20% of the markers had minimal/none motion. The absolute difference in the motion magnitude between the markers, in different locations within the liver, had a positive correlation with the absolute distance between the markers ( $R^2 = 0.69$ , linear-fit). The interfractional gating window varied significantly for some patients, with the largest having 29.4%–56.4% range between fractions.

**Conclusions:** This study analyzed the liver motion characteristics of 20 patients undergoing SBRT. A large variation in motion was observed, interfractionally and intrafractionally, and that as the distance between the markers increased, the difference in the absolute range of motion also increased. This

suggests that marker(s) in closest proximity to the target be used. © 2012 American Association of Physicists in Medicine. [<http://dx.doi.org/10.1118/1.4754658>]

Key words: liver motion, marker tracking, CBCT, IGRT, SBRT

## I. INTRODUCTION

Stereotactic body radiation therapy (SBRT) of liver cancer is technically challenging.<sup>1</sup> Similar to lung cancer, there's a significant interfractional and intrafractional organ motion induced by respiration<sup>2-5</sup> and that radiation tolerance of normal liver is very low.<sup>6-8</sup> The former necessitates a use of larger margin, while the latter discourages it. To make the matter worse, the tumor itself is typically not very distinguishable against the normal liver in in-room cone beam computed tomography (CBCT) imaging, leading to uncertainties in image registration and setup.<sup>9-12</sup>

Since dose-response relationship exists in both primary and metastatic liver cancer, with higher dose resulting in improved outcome,<sup>13,14</sup> the narrowest possible safety margin is prerequisite in maximizing the therapeutic ratio. Consequently, the most accurate and precise target localization technique(s), which minimizes margin size, is essential in liver SBRT. To this end, the use of stereotactic body frame (SBF) and abdominal compression (AC) plate have been popular, in limiting most diaphragm motion to <10 mm.<sup>15-20</sup> Even with reduced motion, however, the problem with image registration uncertainty still remains. An effective solution to this lack of soft tissue contrast is the use of percutaneously inserted fiducial markers as a surrogate.<sup>21-29</sup> This approach is quite effective because the metal markers are radio-opaque and hence are readily visible in x-ray projections. Therefore, using markers to characterize the daily liver motion and subsequently adjusting the treatment setup is an effective strategy in increasing the treatment accuracy.

Having said that, a relatively little is known about the motion variations in the liver, especially within different regions in the organ. In our previous report, we have presented an effective, template-based technique in automatically extracting 2D marker positions from the x-ray projections.<sup>29</sup> In this study, we have used this technique to analyze the motion characteristics of liver. Using 2D positional information at each angular projection as input, we employed a robust 3D motion estimation algorithm to construct the motion traces. From such, we analyzed interfractional and intrafractional motion correlation, correlation with that of the motion acquired during 4DCT simulation, marker-to-marker motion variations within the liver, and variations in the gating window between fractions. With the massive motion information gathered, we systematically deduced useful information that could potentially aid in increasing the overall treatment accuracy of liver SBRT.

## II. MATERIALS AND METHODS

### II.A. Patient data

Twenty liver SBRT patients with hepatocellular carcinoma or metastases at Asan Medical Center (AMC) in Seoul, Korea,

were analyzed. Varian Trilogy linear accelerator (Varian Medical Systems, Palo Alto, CA) with the On-Board Imager (OBI™) was used to acquire CBCT x-ray projections of the patients undergoing 2–8 fractions per course. Images were acquired using the *half-fan* scan mode, where ~650 projections were acquired over the 360° gantry rotation using either the *pelvis* mode (125 kVp, 80 mA, 13 ms/frame) or the *low-dose thorax* mode (110 kVp, 20 mA, 20 ms/frame). The *half-fan* mode is designed to obtain a larger field of view (FOV) of up to 50 cm diameter in axial dimension. In this mode, the detector is shifted laterally and acquires approximately half of the FOV at any projection angle.<sup>29</sup> Each patient had three fiducial markers (2 × 5-mm gold) implanted around the tumor for image guidance. In total, 85 fractions with >55 000 x-ray projections were acquired.

Table I provides the technical details of the patient data. Two to eight fractions were prescribed with three to four being the most popular (accounting for 12/20 cases). One to three markers were embedded in the liver, per patient, with an average of 2.45 markers, with total of 49 markers. The mean marker-to-marker distance was 36.2 mm (range: 1.9–107.5 mm). In terms of CBCT scans, 5/20 patients were imaged with the high-dose *pelvis* mode and 15/20 patients were imaged with the *low-dose thorax* mode.

### II.B. Marker extraction algorithm

We recently proposed a novel template-based marker extraction algorithm.<sup>29</sup> The algorithm is robust against any shape, size, orientation, and the number-of-seeds in an x-ray projection image. Briefly, the algorithm consists of: (1) subsample a small region of interest (ROI) containing all of the markers in the projection image, (2) apply edge enhancement filter using spatial derivatives to highlight the marker features, (3) calculate fast Fourier transform (FFT), enhance the marker-related signals via multiplication with FFT of an ideal marker image, and apply inverse FFT, (4) apply universal threshold to extract the *shadow* of the marker, and finally, (5) calculate the center-of-mass (COM) position of the *shadow*.

For this study, we have modified our algorithm significantly. In the original implementation, we would choose a single ROI that encompasses all of the markers. After that, the algorithm would extract all marker positions inside the ROI, simultaneously. This procedure was efficient when all markers are closely positioned with each other such that the ROI dimension did not exceed about 200 × 200 pixels (77.6 × 77.6 mm), and that patients are scanned with a high quality *pelvis* mode where the markers are clearly distinguishable from the similarly high-attenuating bones and the couch structures, at all scan angles. However, the accuracy of the algorithm fell significantly beyond the ROI dimension of 200

TABLE I. Patient characteristics data. S1–S8 represent the standard liver anatomy segments.

Patient no.	Fractions treated	Observable marker(s)	Intermarker dist. (mm)			Marker location	Imaging protocol
			(1, 2)	(1, 3)	(2, 3)		
1	5	3	2	30	29	S8	<i>Pelvis mode</i>
2	2	3	2	23	22	S4	<i>Pelvis mode</i>
3	7	3	48	30	19	S4, S7	<i>Pelvis mode</i>
4	2	3	27	53	26	S1	<i>Pelvis mode</i>
5	4	3	23	32	22	S8	<i>Pelvis mode</i>
6	8	3	30	95	79	S2	<i>Low-dose thorax</i>
7	3	2	43	–	–	S6, S2	<i>Low-dose thorax</i>
8	3	2	25	–	–	S4	<i>Low-dose thorax</i>
9	8	2	108	–	–	S3, S8	<i>Low-dose thorax</i>
10	3	2	5	–	–	S6	<i>Low-dose thorax</i>
11	4	3	19	27	16	S6, S7	<i>Low-dose thorax</i>
12	3	1	–	–	–	S8	<i>Low-dose thorax</i>
13	4	1	–	–	–	S1	<i>Low-dose thorax</i>
14	4	3	24	40	37	S5	<i>Low-dose thorax</i>
15	4	2	44	–	–	S4, S8	<i>Low-dose thorax</i>
16	5	2	31	–	–	S4, S8	<i>Low-dose thorax</i>
17	3	3	26	24	30	S4	<i>Low-dose thorax</i>
18	6	3	52	33	48	S7	<i>Low-dose thorax</i>
19	3	2	37	–	–	S4	<i>Low-dose thorax</i>
20	4	3	75	91	24	S4	<i>Low-dose thorax</i>

$\times 200$  pixels, as well as when patients were imaged with the *low-dose thorax* mode, where the image noise was higher. To overcome this, we have modified our algorithm/process in that instead of calculating multiple marker positions simultaneously, each marker was calculated separately through assigning a multiple, and much smaller ROIs ( $30 \times 30$  pixels,  $11.64 \times 11.64$  mm). The overall workflow of the marker extraction and the subsequent respiratory signal generation procedures are illustrated in Fig. 1. It is a semiautomatic process where we start by manually assigning the initial position of each marker at the first and the last projections. Then, the marker extraction is performed simultaneously in two opposing directions until either they meet at the last overlapping projection or terminate when the markers are absent. The reason for this approach is that, for the *half-fan* scanning geometry, there are usually a range of scan angles that do not contain the markers due to the off-center position of the detector. This angular range varies from patient to patient and from fraction to fraction, as well as from marker to marker. Therefore, it is efficient to analyze the forward and reverse directions simultaneously and is relatively easy to terminate the process when the markers disappear from the projections. Now, right after manually assigning the marker positions in the first and last projections, a ROI mask of size  $30 \times 30$  pixels is centered on each marker. Then the algorithm determines the COM positions for each image. As the COM positions are determined, the ROI mask is recentered on the new position and the search for the next COM position begins on the subsequent image. This process assumes that the marker from one projection to the next would only move within the ROI area defined. With the typical OBI frame rate of 11–12 frames/s (0.08 s/frame),

we anticipate that this is a reasonable assumption to make unless abnormal abrupt changes occur (e.g., coughing). We have not seen such abrupt changes in our patient cohort. But in the case of such, perhaps it would be wise to omit that portion of the projections in the motion analysis.

### II.C. 3D position estimation algorithm

After identifying the 2D marker positions on all  $>55\,000$  x-ray projection images, each marker was back projected, in the room coordinate system, and the corresponding 3D position was estimated. The main assumption behind this estimation is the prior knowledge that the 3D positions are generally confined within the respiratory/oscillatory trajectory. Assuming that patients are reasonably immobilized during CBCT acquisition, there would be at least two or more projections at different angles that are imaged at the same/similar 3D marker position during the multiple breathing cycles. Therefore, gathering marker positions at all sampled angles would generate a distribution of 3D marker positions that coincide. Since motion is oscillatory, we have assumed that finding the closest point of marker center at a given angle to the central axis of 3D distribution would give a close estimation of the actual marker position in 3D. Such estimation is valid if (1) breathing motion is oscillatory, (2) oscillatory motion is confined to a fixed trajectory, and (3) patient is reasonably immobilized during a CBCT scan. To do this, basically, we project each marker onto *a priori* calculated 3D axial, respiratory motion trajectory, line. And, the 3D axial line is initially calculated by fitting a line that intersects two points that correspond to the average positions of the marker in the

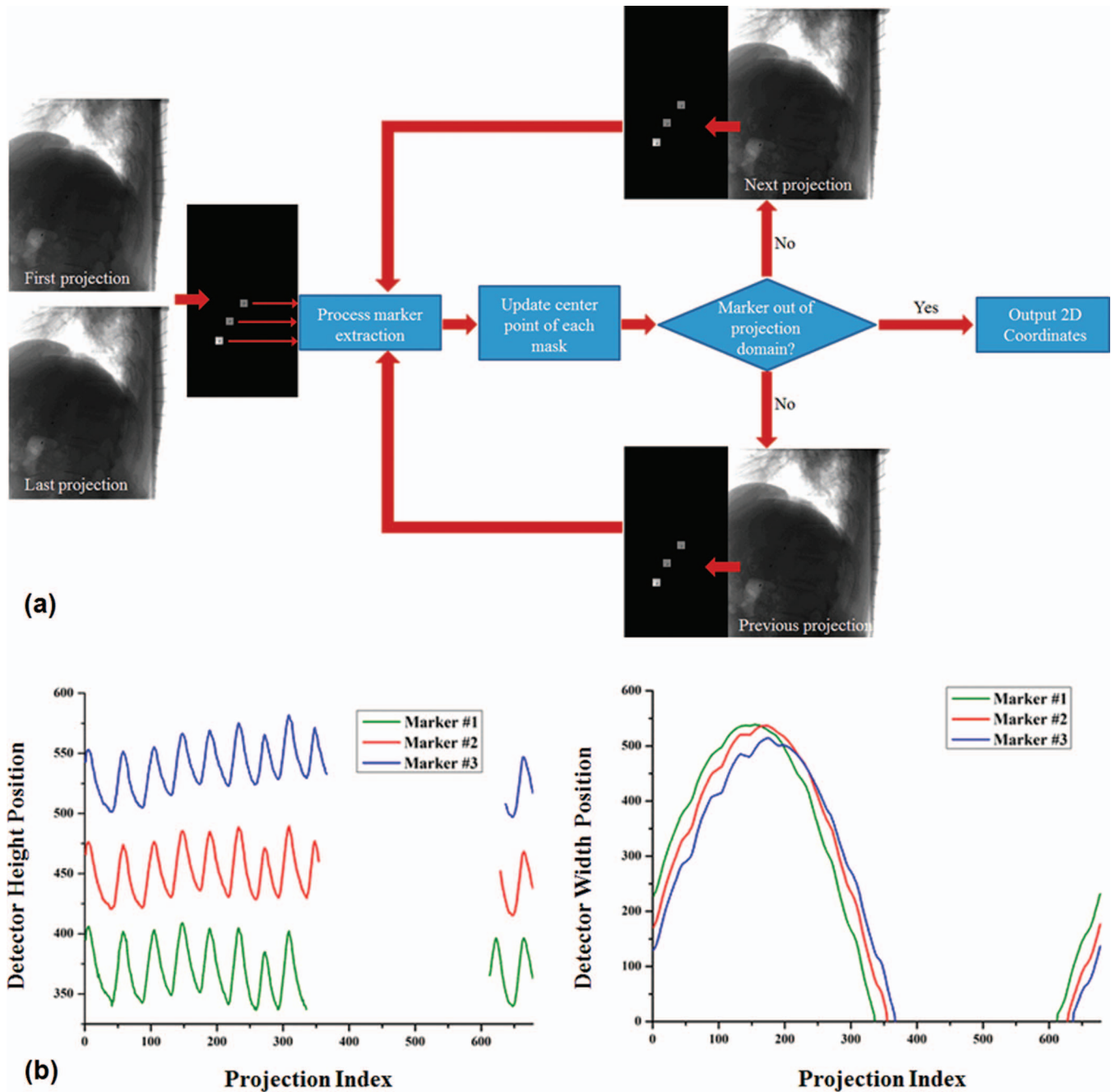


FIG. 1. (a) The overall workflow of the marker extraction process. The extraction is performed simultaneously in the two opposing directions until either they meet at the last overlapping projection or the markers are absent in the image. (b) The height and width positions extracted as a function of the projection angle.

inhalation and exhalation phases. This approach is similar to that proposed by Becker *et al.*<sup>30</sup> where they estimate the 3D position by (1) sorting the marker positions into several phases, (2) each phase is grouped and back projected, (3) an average 3D point of the most-likely intersection is calculated for each phase, and (4) each marker position is then reprojected and the final 3D position is calculated by determining an orthonormal point that is closest to the average 3D position of that phase. Using this approach, the mean root mean square error was  $<0.4$  mm on a phantom study. Once the two average points representing the two phases are calculated, a line vector intersecting the two points are obtained by the following

equation (Fig. 2):

$$f_{\text{axial}}(\mu_{\text{axial}}) = P_{\text{exhal}}(x, y, z) + \mu_{\text{axial}} \cdot (P_{\text{inhal}}(x, y, z) - P(x, y, z)), \quad (1)$$

where variables  $x, y, z, f_{\text{axial}}, P_{\text{exhal}}, P_{\text{inhal}}$ , and  $\mu_{\text{axial}}$  refer to the anterior-posterior (AP) plane, left-right (LR) plane, cranial-caudal (CC) plane, axial line function, average exhalation and inhalation positions, and a scalar weighting variable, respectively. Once the  $f_{\text{axial}}$  is derived, the next step is to project each marker again to calculate the corresponding 3D coordinate position. Projection of the 2D marker position on the detector

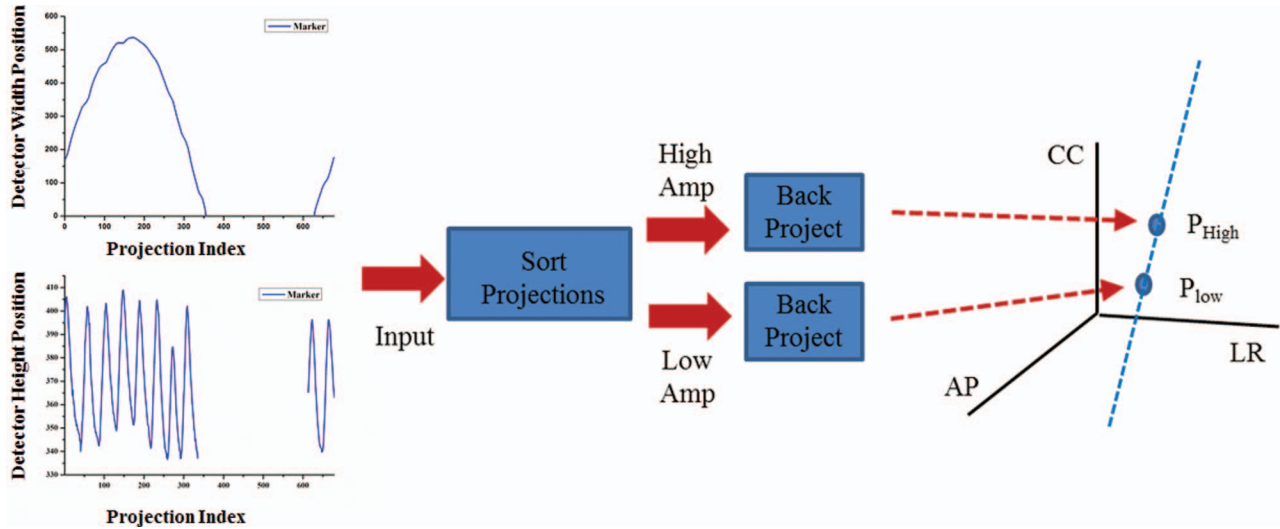


FIG. 2. Illustration of the process in which a 1D respiratory motion trajectory line is obtained. The projections are sorted into either a high-amplitude or low-amplitude signals. Then a line is drawn to intersect the two average points.

plane to a 3D position in the room coordinate space can be first derived by drawing a line vector between the 2D marker positions to the x-ray point source. Mathematically, this can be derived by the following equation:

$$f_{\text{fid}}(\mu_{\text{fid}}) = P_{\text{fid}}(x(\theta), \text{IDD}(\theta), z) + \mu_{\text{fid}} \cdot (P_{\text{src}}(0(\theta), -\text{SID}(\theta), z) - P_{\text{fid}}(x(\theta), \text{IDD}(\theta), z)), \quad (2)$$

where  $f_{\text{fid}}$ ,  $P_{\text{fid}}$ ,  $P_{\text{src}}$ ,  $\text{IDD}$ ,  $\text{SID}$ , and  $\mu_{\text{fid}}$  refer to the projected line vector, the marker position in the detector plane, the x-ray source position, the isocenter-to-detector distance, the x-ray source-to-isocenter distance, and a scalar weighting variable, respectively. Note here that  $x$ ,  $y$ ,  $z$  coordinates are transformed, with respect to the projection angle  $\theta$ , since the gantry rotates during the image acquisition. Finally, using the two line vectors obtained in Eqs. (1) and (2), the ultimate 3D marker position is estimated by calculating an orthonormal point that lies along Eq. (2) line and is closest to Eq. (1) line (Fig. 3). Mathematically, this can be solved using the following equation:

$$f_{3D \text{ pos}}(x, y, z) = \arg \min \| f_{\text{axial}}(\mu_{\text{axial}}) - f_{\text{fid}}(\mu_{\text{fid}}) \|_2^2, \quad (3)$$

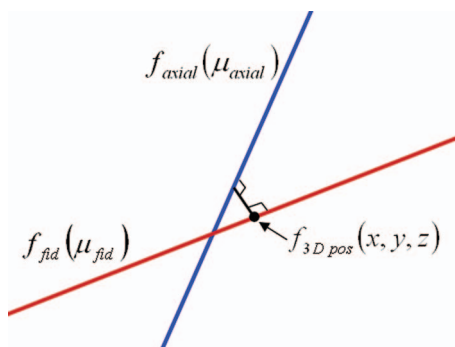


FIG. 3. An illustration of how a 3D marker position is estimated. An orthonormal point along the function  $f_{\text{fid}}$  is calculated that lies closest to the  $f_{\text{axial}}$  line.

where  $f_{3D \text{ pos}}(x, y, z)$  refers to the estimated 3D marker position. Equation (3) can be solved by calculating the derivative with respect to  $\mu_{\text{axial}}$ , setting the equation to zero, and solving for the  $\mu_{\text{fid}}$  that satisfies the equality. This calculation was performed on all markers extracted from the >55 000 projection images.

#### II.D. Data analysis

To analyze the accuracy of our marker tracking algorithm, quantitatively, numerical simulations were performed. First, we analyzed our algorithm using an ideal cosine breathing pattern with constant amplitudes and periods. According to the motion range that we observed from our 4DCT data of the patients, the average amplitude was set to 6, 3, and 16 mm in the AP, LR, and CC directions, respectively. The breathing period was set to 4 s. In the second experiment, we set the amplitudes and periods as in the first experiment but randomly varied the amplitude/period in each breathing cycle in the range of 2–4 mm, 4.5–7.5 mm, and 10–22 mm in AP, LR, and CC directions, respectively, and 2–6 s, to realistically represent the possible variations observed in our patient data. Total of 674 projections of digitally reconstructed radiographs (DRR) were generated per a simulated CBCT scan, in half-fan geometry.

For the patient data, based on the 3D positions estimated, we analyzed a number of liver motion characteristics. First, we evaluated the relative motion tendencies between the three primary directions: LR, AP, and CC. Second, the average and standard deviation of the breathing periods during 4DCT simulation and CBCT scans were calculated. Third, the peak-to-peak motion amplitudes in the LR, AP, and CC directions were calculated. These amplitudes were compared with that of those determined from the maximum intensity projection (MIP) CT images derived from the 4DCT planning dataset. Fourth, the appropriate gating window was retrospectively determined for each fraction. Since the marker motion is

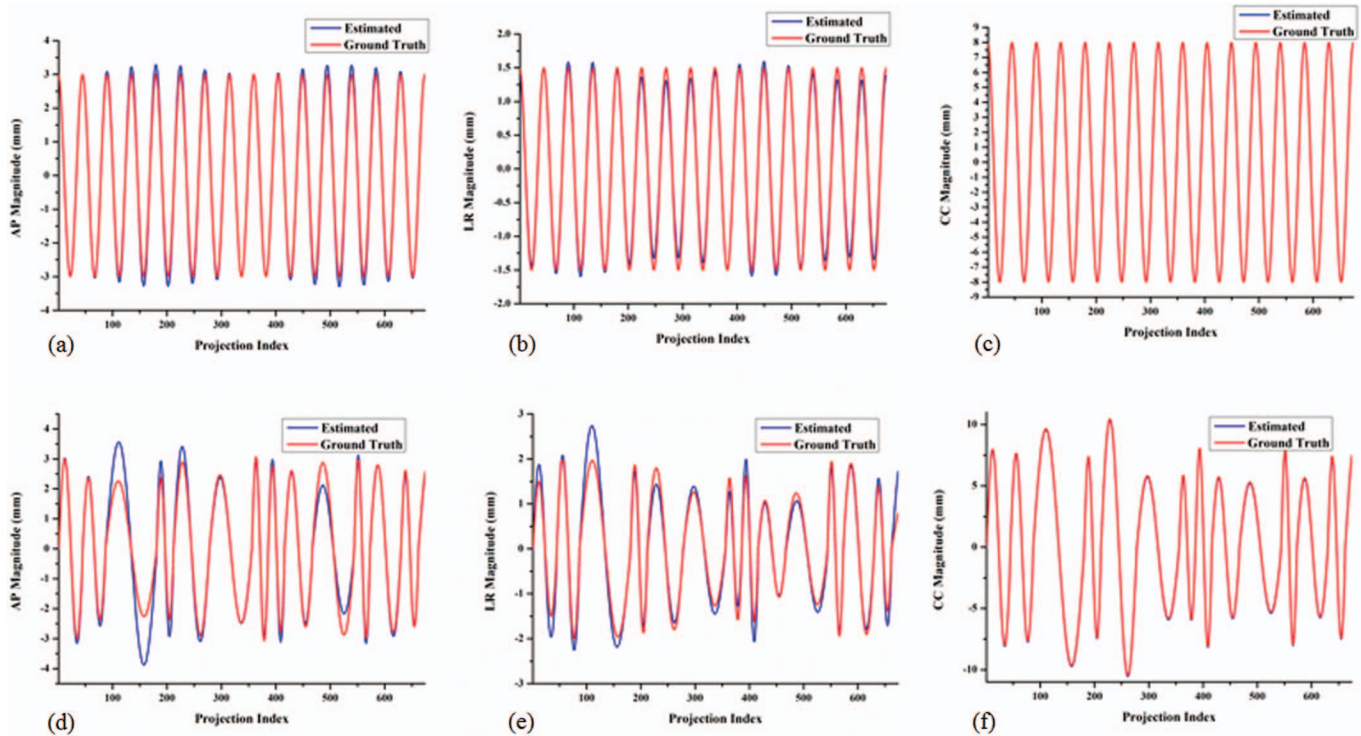


FIG. 4. Comparison of simulated marker tracking results with the ground truth in the AP (a), LR (b), and CC (c) directions with constant breathing, and the AP (d), LR (e), and CC (f) directions with random breathing. Note that CC motion in both cases (c, f) appear to be a single line due to an almost exact overlap with each other.

generally the greatest in the CC direction, a histogram of the marker positions in the CC direction is calculated, for each CBCT scan. Then, the (relative) gating window was defined using the following equation:

$$\text{Gating window}(\%) = \frac{\text{Cumul.Hist.}(50\%) - \text{Min.CC.}}{\text{Max.CC.} - \text{Min.CC.}} \times 100, \quad (4)$$

where Min.CC., Max.CC., and Cumul.Hist.(50%), refer to the most caudal location, the most cranial location, and a median CC ( $z$ ) coordinate position where 50% of the marker positions are below and above. Thus, we define the gating window to be a fraction of the length between the maximum inhalation to the maximum exhalation position that contains half of the marker positions. The algorithms and analysis were implemented on MATLAB (The MathWorks Inc., Natick, MA).

### III. RESULTS

#### III.A. Accuracy of the marker tracking algorithm

Figure 4 shows the results of the marker tracking algorithm accuracy tests where a series of DRRs with moving markers are extracted and tracked in 3D. It appears that the results of marker tracking accuracy are dependent on the randomness of motion. To provide the quantitative accuracy of the results, we have calculated the average relative error of motion in each LR, AP, and CC directions as follows:

$$\text{Relative error}(\%) = \frac{1}{N} \sum_i \frac{(p_i - t_i)^2}{t_i^2} \times 100, \quad (5)$$

where,  $N$ ,  $i$ ,  $p_i$ , and  $t_i$  refer to number of simulated DRRs, projection index number, position of estimated marker position, and position of true marker position, respectively.

It was found that relative errors in the LR, AP, and CC directions were 0.6%, 0.4%, and 0.0% for the first experiment, and 8.0%, 7.1%, and 0.8% for the second experiment. The maximum errors observed were 0.07 mm (LR), 0.2 mm (AP), and 0.002 mm (CC) for the first experiment, and 0.9 mm (LR), 1.6 mm (AP), and 0.1 mm (CC) for the second experiment. The reason that the CC direction results in the smallest errors is that, irrespective of the gantry angle, it is the only direction that is always orthogonal to the x-ray projections, and hence, an accurate position can be obtained always. This is especially true since the detector resolution is very high at  $0.388 \text{ mm}^2$  for the OBI<sup>TM</sup> system.

#### III.B. Liver motion types

Figure 5 shows the orthogonal projection views of all 49 marker trajectories, overlaid on a representative liver contour. As expected, the most dominant motion is in the CC direction. But more interestingly, there is a non-negligible motion in the AP direction as well, irrespective of their location in the liver. Also, the motion in the AP and CC directions are highly correlated. That is, when the markers move cranially, they tend to move posteriorly, and vice versa. The LR motion had a more variable relationship with the AP/CC motions, and appeared random with respect to the location. That is, when the markers moved toward cranial-posterior direction, 58% of the markers moved toward the patient-right (Type I motion), 22% of the

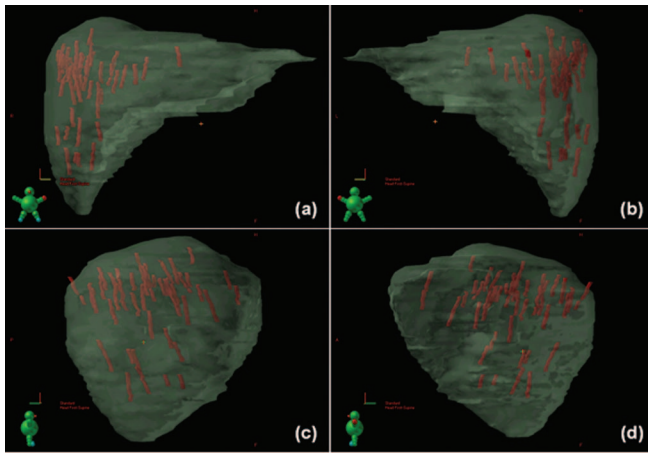


FIG. 5. Trajectories of all 49 markers reconstructed, during their 1st fraction CBCT scans, viewed from the (a) anterior, (b) posterior, (c) left, and (d) right beam's eye view.

markers moved to the patient-left (Type II motion), and 20% of the markers had minimal/none motion (Type III motion). Table II lists the classified motion types for each marker. The motion types were location dependent. Among the 20 patients, only 6/20 patients had all the markers show same type of motion, while 2/20 patients had all markers show different type of motion. The rest of 12/20 patients had markers that were distributed among the three motion classifications. Figure 6 shows the LR motion trajectory of the three markers for a patient (#14 in Table II) illustrating all three different motions.

TABLE II. Three types of motion relationships identified along the LR and the AP/CC directions, that is, when the marker moves toward the cranial-posterior direction, it also moves to the: (Type I) patient-right, (Type II) patient-left, and (Type III) minimal/none motion.

Patient no.	No. of markers in motion		
	Type I	Type II	Type III
1	3	–	–
2	3	–	–
3	1	–	2
4	1	2	–
5	3	–	–
6	–	1	2
7	–	1	1
8	2	–	–
9	–	1	1
10	2	–	–
11	3	–	–
12	–	–	1
13	1	–	–
14	1	1	1
15	1	–	1
16	1	–	1
17	3	–	–
18	1	1	1
19	2	–	–
20	–	3	–

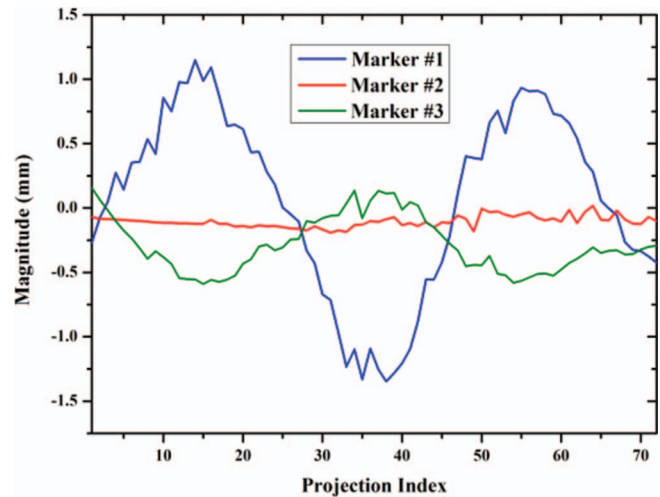


FIG. 6. An example patient showing the three types of LR motion with the corresponding three markers implanted.

### III.C. Liver motion variability

Table III lists the comprehensive peak-to-peak amplitude, across the three dimensions, and the breathing period observed during the 4DCT simulation and the CBCT scans. Breathing period during the 4DCT scans was recorded by the RPM™ system (Varian Medical Systems, Palo Alto, CA). As observed, the CC and LR directions were generally the most and least dominant motions, respectively, except one patient (#9, Marker #1) where the LR motion was significantly larger than the AP motion. The range of motion for the 20 patients were  $3.0 \pm 2.0$  mm,  $5.1 \pm 3.1$  mm, and  $17.9 \pm 5.1$  mm in the planning 4DCT, and  $2.8 \pm 1.6$  mm,  $5.3 \pm 3.1$  mm, and  $16.5 \pm 5.7$  mm in the treatment CBCT, for LR, AP, and CC directions, respectively. The range of respiratory period was  $3.9 \pm 0.7$  and  $4.2 \pm 0.8$  s during the 4DCT simulation and the CBCT scans, respectively. Some patients had a considerable disparity in motion characteristics between the simulation and treatment. The absolute difference in the motion magnitude ranged from 0 to 8.6 mm, 0 to 6.8 mm, and 0.2 to 9.3 mm across LR, AP, and CC directions, respectively. Correspondingly, the absolute mean difference was  $0.9 \pm 1.3$  mm,  $1.0 \pm 1.1$  mm, and  $3.4 \pm 2.6$  mm, respectively. It was observed that 4/20 patients had absolute motion difference in the CC direction of at least  $>5$  mm for all markers embedded. 8/20 (40%) patients had the mean motion smaller during the CBCT scans than the 4DCT simulation, while 3/20 (15%) patients had the mean motion greater by at least 2 mm or larger. Change in breathing pattern from during the 4DCT simulation to the CBCT scans ranged from  $-2.0$  to  $+1.0$  s, with an average of  $-0.2 \pm 0.8$  s.

Figure 7 illustrates interfractional and intrafractional motion variability, in CC direction, of four representative patients. As observed, there are considerable variations in the majority of patients [Fig. 7(a)–7(c)]. Not only is the peak-to-peak amplitude changing between fractions, the intrafractional breathing pattern also varies significantly [Fig. 7(c), Fraction 1]. And, unless the image registration between the 4DCT (MIP) and CBCT is accurate, sometimes, the

TABLE III. The comprehensive list of peak-to-peak amplitude, across the three dimensions, and the breathing period observed during the 4DCT simulation and the CBCT scans. The two cases with the most significant intermarker motion variations are underlined.

Patient no.	Modality	Mean amplitude (mm $\pm$ SD)									Breathing period (Sec $\pm$ SD)
		Marker 1			Marker 2			Marker 3			
		LR	AP	CC	LR	AP	CC	LR	AP	CC	
1	MIP	5.4	9.0	27.5	4.4	9.9	27.5	2.8	8.1	25.0	5.2 (0.5)
	OBI	3.1 (0.5)	10.3 (1.5)	32.4 (3.3)	3.1 (0.6)	10.3 (1.6)	32.4 (3.2)	3.5 (0.7)	9.8 (1.3)	30.1 (3.6)	5.2 (0.4)
2	MIP	2.9	2.8	10.0	2.0	3.7	10.0	1.8	3.8	10.0	4.2 (0.4)
	OBI	2.4 (0.7)	3.9 (0.6)	12.1 (1.2)	2.4 (0.7)	3.9 (0.6)	12.1 (1.2)	2.2 (0.4)	3.8 (0.5)	12.3 (1.1)	3.6 (0.5)
3	MIP	2.8	5.5	12.5	1.0	3.7	12.5	1.0	3.7	12.5	3.9 (0.7)
	OBI	2.2 (0.5)	3.5 (0.6)	9.6 (1.4)	1.3 (0.6)	2.5 (0.6)	8.2 (1.6)	1.1 (0.6)	3.1 (0.5)	9.1 (1.3)	3.2 (0.6)
4	MIP	2.5	6.7	17.5	1.0	5.9	17.5	2.5	5.9	15.0	3.8 (0.5)
	OBI	1.1 (0.4)	6.4 (0.8)	16.8 (1.4)	1.8 (0.4)	7.0 (1.1)	16.4 (1.3)	3.7 (0.7)	7.1 (1.5)	13.6 (2.1)	3.9 (0.4)
5	MIP	3.5	3.5	25.0	1.0	3.5	22.5	1.0	2.6	22.5	4.8 (0.6)
	OBI	1.5 (0.4)	2.4 (0.4)	15.8 (1.0)	1.1 (0.4)	2.3 (0.7)	14.8 (1.0)	1.1 (0.3)	2.9 (0.5)	15.6 (1.1)	3.7 (0.4)
6	MIP	1.0	5.9	17.5	1.0	3.9	17.5	2.9	3.9	17.5	4.0 (0.1)
	OBI	0.9 (0.3)	6.4 (0.7)	18.6 (1.2)	1.0 (0.3)	6.5 (0.6)	19.1 (1.3)	3.4 (0.7)	3.1 (0.6)	19.0 (1.4)	4.6 (0.4)
7	MIP	2.4	4.7	25.0	1.0	4.7	22.5	1.0	5.7	22.5	3.6 (0.1)
	OBI	2.9 (0.3)	5.9 (0.4)	18.6 (1.3)	1.1 (0.8)	5.8 (0.4)	18.3 (0.9)		N/A		3.9 (0.3)
8	MIP	1.9	1.9	10.0	1.9	2.9	10.0	1.9	6.5	17.5	3.7 (0.1)
	OBI	2.5 (0.4)	2.1 (0.6)	11.7 (0.7)	4.1 (1.4)	2.7 (0.8)	10.6 (0.9)		N/A		4.2 (0.2)
9	MIP	<u>5.7</u>	<u>1.0</u>	<u>10.0</u>	<u>2.8</u>	<u>1.8</u>	<u>20.0</u>	1.9	4.8	20.0	4.2 (0.3)
	OBI	<u>5.8 (1.1)</u>	<u>1.2 (0.5)</u>	<u>8.0 (0.8)</u>	<u>1.1 (0.4)</u>	<u>2.1 (0.6)</u>	<u>17.2 (1.8)</u>		N/A		4.5 (0.8)
10	MIP	8.8	13.3	22.5	7.1	16.8	25.0	6.2	15.9	25.0	4.6 (0.2)
	OBI	6.0 (0.3)	12.6 (0.8)	21.0 (1.3)	7.0 (5.6)	16.3 (0.8)	23.6 (1.7)		N/A		4.7 (0.3)
11	MIP	3.8	3.8	20.0	4.7	3.8	17.5	3.8	3.8	17.5	3.9 (0.1)
	OBI	4.1 (0.3)	4.2 (0.2)	20.6 (0.9)	3.9 (0.5)	3.7 (0.8)	17.4 (1.1)	3.7 (0.3)	3.6 (0.4)	16.8 (1.0)	4.3 (0.4)
12	MIP	1.7	5.4	12.5	2.6	3.5	10.0	5.3	3.5	12.5	4.1 (0.1)
	OBI	1.2 (0.7)	5.4 (0.7)	10.6 (1.1)		N/A			N/A		4.2 (0.3)
13	MIP	3.2	5.2	20.0	8.6	4.3	22.5	6.9	5.2	17.5	3.5 (0.1)
	OBI	3.4 (0.5)	5.4 (0.7)	17.5 (1.5)		N/A			N/A		3.5 (0.3)
14	MIP	1.9	4.6	17.5	1.0	5.5	20.0	1.9	5.6	22.5	3.9 (0.1)
	OBI	2.0 (0.4)	3.7 (0.5)	15.5 (1.2)	0.9 (0.4)	3.7 (0.8)	14.9 (1.2)	0.9 (0.3)	5.5 (1.7)	15.2 (1.2)	3.6 (0.3)
15	MIP	2.7	1.0	15.0	1.0	2.7	12.5	1.0	2.7	25.0	4.6 (0.3)
	OBI	4.2 (0.4)	7.8 (0.8)	23.4 (1.3)	2.1 (0.6)	5.4 (0.3)	21.8 (1.4)		N/A		6.0 (0.2)
16	MIP	2.7	6.2	15.0	1.9	9.8	17.5	1.0	8.0	17.5	3.6 (0.5)
	OBI	2.3 (0.4)	8.2 (1.0)	16.1 (1.6)	1.4 (0.5)	7.9 (1.0)	15.2 (1.7)		N/A		3.3 (0.4)
17	MIP	4.3	3.4	15.0	4.3	3.4	15.0	6.3	3.4	15.0	3.1 (0.1)
	OBI	4.8 (1.2)	5.2 (0.5)	12.8 (1.0)	4.7 (0.9)	4.1 (0.8)	14.1 (0.9)	5.7 (1.1)	3.2 (0.4)	13.0 (1.4)	5.1 (0.6)
18	MIP	1.0	2.5	17.5	5.0	3.3	22.5	1.0	2.5	17.5	2.1 (0.2)
	OBI	1.9 (0.5)	2.5 (0.6)	12.4 (2.0)	3.1 (0.7)	3.6 (0.8)	16.5 (3.5)	1.0 (0.4)	2.0 (0.6)	11.8 (1.9)	3.3 (0.6)
19	MIP	4.5	4.5	17.5	3.6	4.5	17.5	3.6	5.4	17.5	4.2 (0.1)
	OBI	2.9 (0.3)	3.2 (0.6)	11.3 (1.1)	2.3 (0.5)	3.8 (0.7)	10.2 (1.2)		N/A		3.3 (0.2)
20	MIP	<u>1.7</u>	<u>3.4</u>	<u>15.0</u>	<u>4.3</u>	<u>6.8</u>	<u>25.0</u>	<u>5.1</u>	<u>8.5</u>	<u>27.5</u>	4.5 (0.3)
	OBI	<u>1.9 (0.5)</u>	<u>4.0 (0.6)</u>	<u>14.4 (0.9)</u>	<u>4.5 (0.4)</u>	<u>9.2 (0.6)</u>	<u>23.6 (1.3)</u>	<u>5.9 (0.5)</u>	<u>10.5 (0.7)</u>	<u>24.9 (1.6)</u>	4.5 (0.4)

motion magnitude extends out of the margin observed in the planning MIP CT, for a significant proportion of the time [Fig. 7(a), Fractions 2–5]. The most extreme case is observed in Fig. 7(c), Fraction 1, where up to 1 cm (sudden) shift in the baseline is seen accompanied by a severe irregularity in the breathing pattern. For this fraction, >7 mm deviation out of the MIP margin was observed, potentially compromising the SBRT accuracy significantly.

The variability in the interfractional motion is nicely captured by the necessary gating window needed for each fraction, as illustrated in Fig. 8. For some patients, the fractional

change in the gating window was quite significant (>20% for Patients #3, #5, #13, #14, #15, and #18), with the largest having 29.5%–56.4% range between fractions (Patient #14). In all, the gating window ranged between 16.3% and 56.5%, for the population.

The marker-to-marker motion variability, within different locations in the liver, was also significant in some cases. Two most significant cases are underlined in Table III (Patients #9 and #20). As can be seen, the difference in the motion magnitude between the markers is nearly 1 cm, in the CC direction. Figure 9 shows the Patient #20 motion trajectory

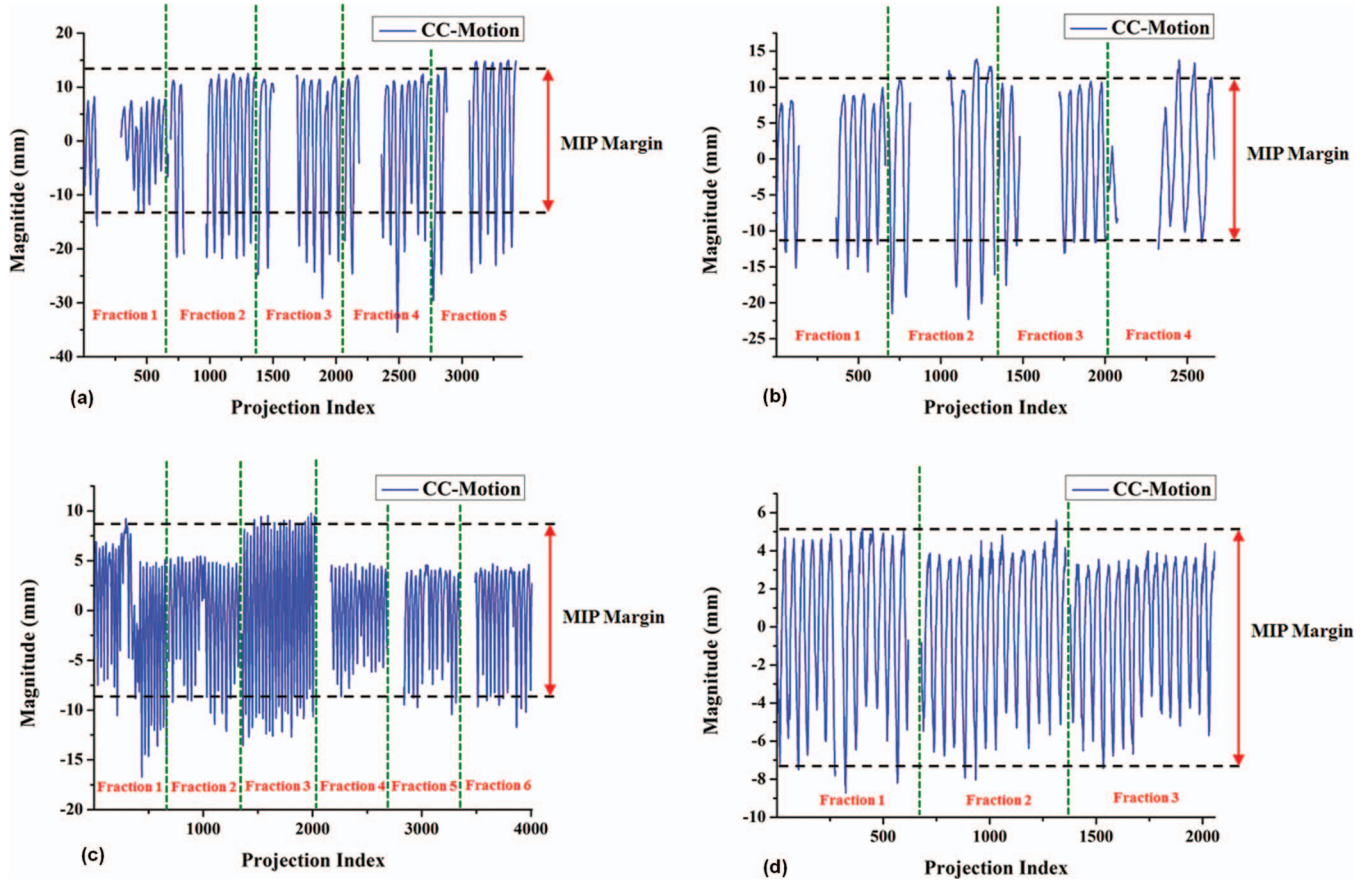


FIG. 7. Four representative patients illustrating the typical interfractional and intrafractional motion variations: (a) Patient #1, (b) Patient #14, (c) Patient #18, and (d) Patient #12. Also shown is the “MIP margin” motion range determined by the planning MIP CT.

between the two markers. It is evident that, at all three directions, the motion magnitude differences are great, with the Marker #3 having a predominantly larger motion. Figure 10 illustrates a clear trend in the absolute difference in the motion magnitude between the markers as the distance increases

( $R^2 = 0.69$ , linear-fit). This suggests that marker(s) in closest proximity to the target should bear more weight when performing image registration for patient setup, which also suggests that the markers should be implanted as close as possible to the gross tumor.

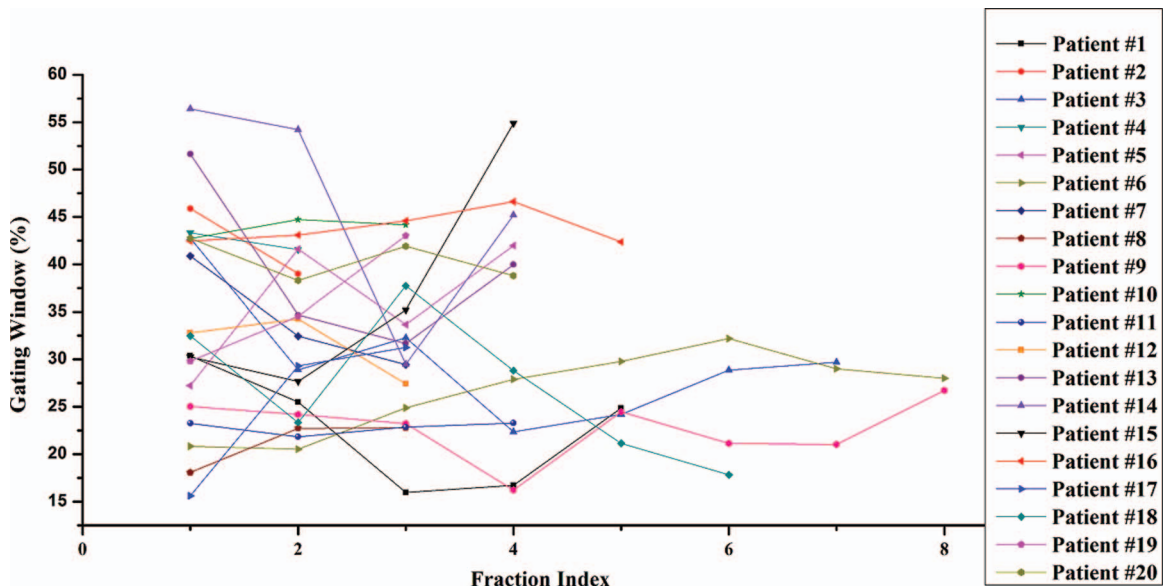


FIG. 8. The appropriate % gating window determined based on the marker motion trajectory of each fraction, for each patient.

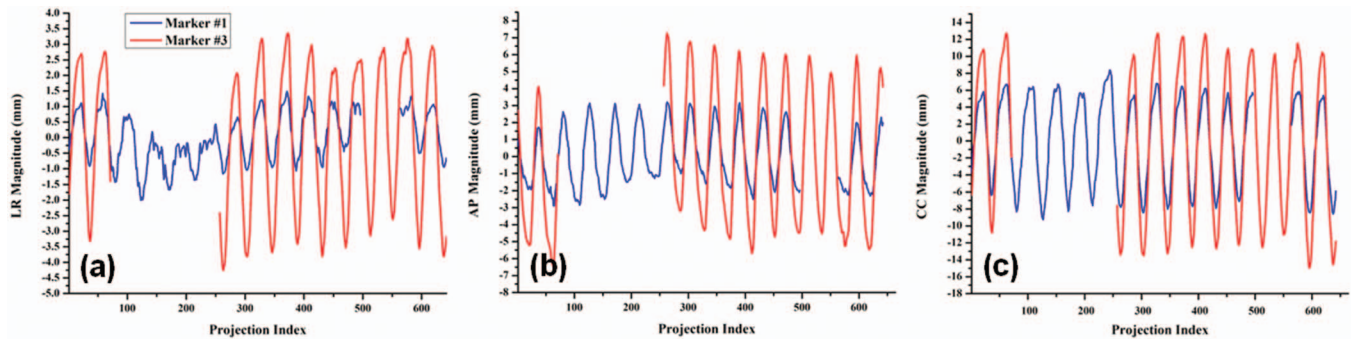


FIG. 9. The intermarker motion variability in the (a) LR, (b) AP, and (c) CC directions, for Patient #20.

## IV. DISCUSSION

### IV.A. 3D motion tracking

In liver SBRT, the fiducial markers are important due to the fact that (1) the tumor contrast is very low in the CBCT images, and (2) the motion induced by respiration is significant. This is why liver motion characterization studies have been largely performed with the markers in the past,<sup>11,12,17</sup> including with the RTRT system in Japan.<sup>4,5,21–25</sup> For the RTRT system, using fluoroscopic imaging with multiple x-rays, the precise 3D marker positions can be extracted near real-time with submillimeter accuracy. Another predominant feature is that it is able to track/verify such information at all/most time during treatment. However, of course, the cost of employing such a design is the added imaging dose.

In this study, we have demonstrated that CBCT x-ray projection images can also be used to track and verify the 3D motion trajectories, as has some investigators in the past.<sup>30–32</sup> However, to the best of our knowledge, the use of the projections to study the motion characteristics of the liver have not been rigorously studied yet. The main advantages of utilizing the projection images are that, first, it does not require additional hardware (if you have a CBCT system on your linear accelerator), and second, that the same projection data can be used to reconstruct a 3D image volume for image-guided radiotherapy (IGRT), thus avoiding extra imaging dose to patients. Although the projection images do not provide real-

time motion information during treatment, like as in the RTRT or the CyberKnife<sup>TM</sup> systems (AccuRay, Sunnyvale, CA), the motion data it does provide, prior to the treatment, is still very valuable in understanding and guiding the patient set up,<sup>30–32</sup> for 4DCBCT reconstructions,<sup>29</sup> and potentially useful in various adaptive radiotherapy (ART) strategies.

In this study, a sizable portion of the markers could not be used for analysis (in 9/20 patients, only 1–2 markers were tracked, see Table I), even though all patients had three markers implanted each. There were three main reasons for this. First, in the *half-fan* scanning geometry, due to the off-centering of the detector panel, there occasionally exist too large of scan angles with the markers being outside of the FOV. Second, some markers were too cranially or caudally located from the isocenter and thus did not appear in the projection images. And, finally, since a large portion of the patients was imaged with the *low-dose thorax* mode (15/20 patients), some projection images were just too noisy to allow visualization of the markers (Fig. 11).

On validating the accuracy of our modified marker tracking algorithm, we have limited our investigation to a cosine type breathing pattern. It was found that the relative error in all directions were  $<1\%$  when amplitude is fixed and  $<8\%$  when amplitude is randomly varying. Moreover, the results showed that the relative motion error in the CC direction (motion perpendicular to the projection orientation) was significantly less than either in the LR or AP directions (motion along the projection orientation). This has also been observed in an earlier

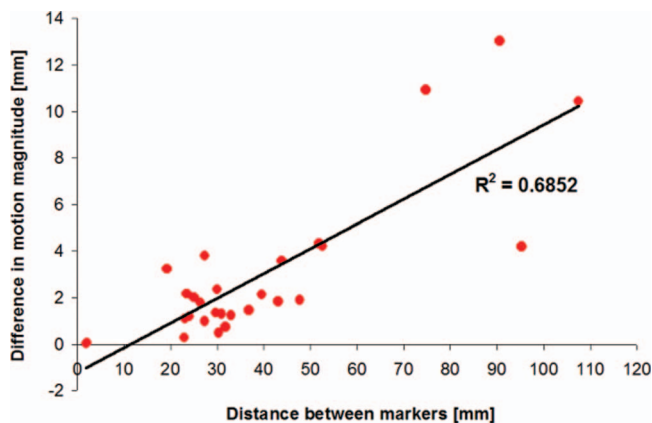


FIG. 10. Scatter plot showing the absolute intermarker motion magnitude difference as a function of the marker-to-marker separation.

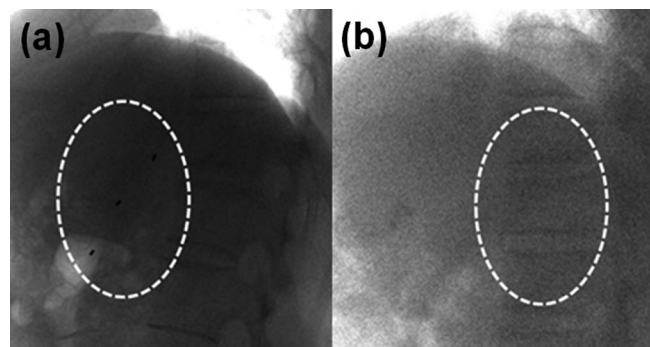


FIG. 11. Typical projection images taken with the (a) *pelvis* mode, and the (b) *low-dose thorax* mode. The white dotted circles indicate where the markers should be located.

work as well.<sup>30</sup> Remember that our marker tracking algorithm is based on the prior knowledge of oscillatory 3D marker positions calculated from the 2D marker positions at different projection angles. On running position estimation algorithm, we have assumed that fiducial marker motion is oscillatory with confined axis of rotation. Therefore, it is logical that more consistent and regular the breathing pattern the tracking process would be more accurate. If patient breathing pattern is subjected to abrupt change such as cough, it is expected that uncertainty of position would also increase. It is shown in this study that as motion irregularity gets severe, uncertainty of tracking would also increase due to the fact that the accuracy of *a priori* calculated 3D axial line is to large extent dependent upon regularity of breathing.

In this study, we have limited our investigation to a single fiducial marker design of cylindrical shape ( $2 \times 5$ -mm gold). However, we anticipate that our marker extraction as well as modified tracking algorithm would work as accurate as for different shaped or sized markers, as long as the features of the marker are clearly visible and extractable from the CBCT projections.<sup>29</sup>

#### IV.B. Liver motion

Our results indicate that, in general, the liver motion is most dominant in the CC direction, followed by the AP direction, and the LR direction. In one exceptional case (Patient #9, Marker #1), we found that the LR motion magnitude was significantly larger than the AP motion magnitude (5.8 vs 1.2 mm). In addition, the motion in the AP and CC directions were highly correlated, where, when the markers moved cranially, they moved posteriorly, and vice versa. The LR motion, however, had a more variable relationship with the AP/CC motions, and appeared random with respect to the location. Thus, since there are some correlations and some randomness to the liver motion, this suggests that a careful attention is needed in characterizing the tumor motion during the planning and the treatment processes.

There was significant motion variability observed between the 4DCT and the CBCT scans. The absolute difference in the motion magnitude ranged from 0 to 8.6 mm, 0 to 6.8 mm, and 0.2 to 9.3 mm across LR, AP, and CC directions, respectively. It was observed that 4/20 patients had absolute motion difference in the CC direction of at least  $>5$  mm for all markers implanted. Changes in breathing period ranged from  $-2.0$  to  $+1.0$  s, with an average of  $-0.2 \pm 0.8$  s. This suggests that, for some patients, the planning 4DCT images do not accurately represent the patient motion characteristics throughout the treatments. In addition, a recent study by Vergalasova *et al.*<sup>33</sup> points out that a free-breathing 3DCBCT is very limited in capturing the full range of motion, and that the appearance of the motion-blurred ITV is heavily dependent on the breathing pattern of the day. With this, and since Fig. 7 has shown the range of possible interfractional and intrafractional variability that can be observed in the liver motion, this strongly suggests that free-breathing 3DCBCT scans may not be accurate enough in guiding the liver SBRT treatments, even

with the markers implanted. Perhaps the best solution is to take 4DCBCT scans for all fractions.<sup>29</sup>

We also found that the motion pattern and magnitude depends strongly on the location within the liver. As Fig. 10 has shown, the motion magnitude tends to be different as the distance between the markers increased. This finding is consistent with the previous works<sup>11,12</sup> where the accuracy of the tumor position prediction decreases with the increasing distance between the implanted markers and the tumor. Specifically, from Fig. 10, it can be observed that when marker separation is about  $\sim 5.5$  cm or greater, the difference in motion magnitude starts to exceed 5 mm. Thus, although the closer the better, it is advisable to use markers located closer than about 5 cm to expect deviations  $<5$  mm, while avoiding implanting directly in the tumor to avoid possible spread of tumor cells.

#### V. CONCLUSION

This study analyzed the liver motion characteristics of 20 patients undergoing SBRT. A large variation in motion was observed, interfractionally and intrafractionally, and that as the distance between the markers increased, the difference in the absolute range of motion also increased. This suggests that marker(s) in closest proximity to the target be used.

#### ACKNOWLEDGMENTS

This project was supported by Varian Medical Systems and Radiation Safety Programs (2011-31115, 19192) through the National Research Foundation. The authors report no conflicts of interest in conducting the research.

<sup>a</sup>Electronic mail: michael@amc.seoul.kr; Telephone: +82-2-3010-4433; Fax: +82-2-3010-6950.

<sup>b</sup>Also at Department of Radiation Medicine and Applied Sciences, University of California San Diego, Rebecca and John Moores Comprehensive Cancer Center, 3855 Health Sciences Drive #0843, La Jolla, California 92093-0843. Electronic mail: wysong@ucsd.edu; Telephone: +1-858-246-0886; Fax: +1-858-822-5568.

<sup>1</sup>S. H. Benedict, K. M. Yenice, D. Followill, J. M. Galvin, W. Hinson, B. Kavanagh, P. Keall, M. Lovelock, S. Meeks, L. Papiez, T. Purdie, R. Sadagopan, M. C. Schell, B. Salter, D. J. Schlesinger, A. S. Shiu, T. Solberg, D. Y. Song, V. Stieber, R. Timmerman, W. A. Tome, D. Verellen, L. Wang, and F. F. Yin, "Stereotactic body radiation therapy: The report of AAPM Task Group 101," *Med. Phys.* **37**(8), 4078–4101 (2010).

<sup>2</sup>R. B. Case, D. J. Moseley, J. J. Sonke, C. L. Eccles, R. E. Dinniwel, J. Kim, A. Bezjak, M. Milosevic, K. K. Brock, and L. A. Dawson, "Interfraction and intrafraction changes in amplitude of breathing motion in stereotactic liver radiotherapy," *Int. J. Radiat. Oncol., Biol., Phys.* **77**(3), 918–925 (2010).

<sup>3</sup>R. B. Case, J. J. Sonke, D. J. Moseley, J. Kim, K. K. Brock, and L. A. Dawson, "Inter- and intrafraction variability in liver position in non-breath-hold stereotactic body radiotherapy," *Int. J. Radiat. Oncol., Biol., Phys.* **75**(1), 302–308 (2009).

<sup>4</sup>K. Kitamura, H. Shirato, Y. Seppenwoolde, T. Shimizu, Y. Kodama, H. Endo, R. Onimaru, M. Oda, K. Fujita, S. Shimizu, and K. Miyasaka, "Tumor location, cirrhosis, and surgical history contribute to tumor movement in the liver, as measured during stereotactic irradiation using a real-time tumor-tracking radiotherapy system," *Int. J. Radiat. Oncol., Biol., Phys.* **56**(1), 221–228 (2003).

<sup>5</sup>T. Nishioka, S. Nishioka, M. Kawahara, S. Tanaka, H. Shirato, K. Nishi, and T. Hiromura, "Synchronous monitoring of external/internal respiratory

- motion: validity of respiration-gated radiotherapy for liver tumors," *Jpn. J. Radiol.* **27**(7), 285–289 (2009).
- <sup>6</sup>C. C. Pan, B. D. Kavanagh, L. A. Dawson, X. A. Li, S. K. Das, M. Miften, and R. K. Ten Haken, "Radiation-associated liver injury," *Int. J. Radiat. Oncol., Biol., Phys.* **76**(3), S93–S99 (2010).
  - <sup>7</sup>L. A. Dawson, D. Normolle, J. M. Balter, C. J. McGinn, T. S. Lawrence, and R. K. Ten Haken, "Analysis of radiation induced liver disease using the Lyman NTCP model," *Int. J. Radiat. Oncol., Biol., Phys.* **53**(4), 810–821 (2002).
  - <sup>8</sup>L. A. Dawson, C. Eccles, and T. Craig, "Individualized image guided iso-NTCP based liver cancer SBRT," *Acta Oncol.* **45**(7), 856–864 (2006).
  - <sup>9</sup>R. Case, D. Moseley, J. P. Bissonnette, J. Kim, and L. Dawson, "Variability in the amplitude of liver motion in patients undergoing cone-beam CT image-guided free breathing stereotactic body radiotherapy," *Radiother. Oncol.* **84**, S38–S38 (2007).
  - <sup>10</sup>M. Romero, R. T. Zinkstok, W. Wunderink, R. M. van Os, H. Joosten, Y. Seppenwoolde, P. J. C. M. Nowak, R. P. Brandwijk, C. Verhoef, J. N. M. Ijzermans, P. C. Levendag, and B. J. M. Heijmen, "Stereotactic body radiation therapy for liver tumors: Impact of daily setup corrections and day-to-day anatomic variations on dose in target and organs at risk," *Int. J. Radiat. Oncol., Biol., Phys.* **75**(4), 1201–1208 (2009).
  - <sup>11</sup>W. Wunderink, A. Mendez Romero, Y. Seppenwoolde, H. de Boer, P. Levendag, and B. Heijmen, "Potentials and limitations of guiding liver stereotactic body radiation therapy set-up on liver-implanted fiducial markers," *Int. J. Radiat. Oncol., Biol., Phys.* **77**(5), 1573–1583 (2010).
  - <sup>12</sup>Y. Seppenwoolde, W. Wunderink, W. R. Wunderink-van Veen, P. Storchi, A. Mendez Romero, and B. J. M. Heijmen, "Treatment precision of image-guided liver SBRT using implanted fiducial markers depends on marker-tumour distance," *Phys. Med. Biol.* **56**(17), 5445–5468 (2011).
  - <sup>13</sup>R. McCammon, T. Scheffer, R. Zaemisch, D. Gradvahl, and B. Kavanagh, "Improved local control associated with dose-escalated stereotactic body radiation therapy (SBRT) indicates dose-response relationship," *Int. J. Radiat. Oncol., Biol., Phys.* **69**(3), S152–S153 (2007).
  - <sup>14</sup>W. Park, D. H. Lim, S. W. Paik, K. C. Koh, M. S. Choi, C. K. Park, B. C. Yoo, J. E. Lee, M. K. Kang, Y. J. Park, H. R. Nam, Y. C. Ahn, and S. J. Huh, "Local radiotherapy for patients with unresectable hepatocellular carcinoma," *Int. J. Radiat. Oncol., Biol., Phys.* **61**(4), 1143–1150 (2005).
  - <sup>15</sup>C. L. Eccles, L. A. Dawson, J. L. Moseley, and K. K. Brock, "Interfraction liver shape variability and impact on GTV position during liver stereotactic radiotherapy using abdominal compression," *Int. J. Radiat. Oncol., Biol., Phys.* **80**(3), 938–946 (2011).
  - <sup>16</sup>J. H. Heinzerling, J. F. Anderson, L. Papiez, T. Boike, S. Chien, G. Zhang, R. Abdulrahman, and R. Timmerman, "Four-dimensional computed tomography scan analysis of tumor and organ motion at varying levels of abdominal compression during stereotactic treatment of lung and liver," *Int. J. Radiat. Oncol., Biol., Phys.* **70**(5), 1571–1578 (2008).
  - <sup>17</sup>W. Wunderink, A. Mendez Romero, W. de Kruijff, H. de Boer, P. Levendag, and B. Heijmen, "Reduction of respiratory liver tumor motion by abdominal compression in stereotactic body frame, analyzed by tracking fiducial markers implanted in liver," *Int. J. Radiat. Oncol., Biol., Phys.* **71**(3), 907–915 (2008).
  - <sup>18</sup>K. K. Herfarth, J. Debus, F. Lohr, M. L. Bahner, P. Fritz, A. Hoss, W. Schlegel, and M. F. Wannemacher, "Extracranial stereotactic radiation therapy: set-up accuracy of patients treated for liver metastases," *Int. J. Radiat. Oncol., Biol., Phys.* **46**(2), 329–335 (2000).
  - <sup>19</sup>J. Wulf, U. Hadinger, U. Oppitz, B. Olshausen, and M. Flentje, "Stereotactic radiotherapy of extracranial targets: CT-simulation and accuracy of treatment in the stereotactic body frame," *J. Clin. Oncol.* **57**(2), 225–236 (2000).
  - <sup>20</sup>J. Wulf, U. Hadinger, U. Oppitz, W. Thiele, and M. Flentje, "Impact of target reproducibility on tumor dose in stereotactic radiotherapy of targets in the lung and liver," *J. Clin. Oncol.* **66**(2), 141–150 (2003).
  - <sup>21</sup>K. Kitamura, H. Shirato, S. Shimizu, N. Shinohara, T. Harabayashi, T. Shimizu, Y. Kodama, H. Endo, R. Onimaru, S. Nishioka, H. Aoyama, K. Tsuchiya, and K. Miyasaka, "Registration accuracy and possible migration of internal fiducial gold marker implanted in prostate and liver treated with real-time tumor-tracking radiation therapy (RTRT)," *J. Clin. Oncol.* **62**(3), 275–281 (2002).
  - <sup>22</sup>H. Shirato, T. Harada, T. Harabayashi, K. Hida, H. Endo, K. Kitamura, R. Onimaru, K. Yamazaki, N. Kurauchi, T. Shimizu, N. Shinohara, M. Matsushita, H. Dosaka-Akita, and K. Miyasaka, "Feasibility of insertion/implantation of 2.0-mm-diameter gold internal fiducial markers for precise setup and real-time tumor tracking in radiotherapy," *Int. J. Radiat. Oncol., Biol., Phys.* **56**(1), 240–247 (2003).
  - <sup>23</sup>H. Shirato, M. Oita, K. Fujita, Y. Watanabe, and K. Miyasaka, "Feasibility of synchronization of real-time tumor-tracking radiotherapy and intensity-modulated radiotherapy from viewpoint of excessive dose from fluoroscopy," *Int. J. Radiat. Oncol., Biol., Phys.* **60**(1), 335–341 (2004).
  - <sup>24</sup>H. Shirato, S. Shimizu, K. Kitamura, T. Nishioka, K. Kagei, S. Hashimoto, H. Aoyama, T. Kunieda, N. Shinohara, H. Dosaka-Akita, and K. Miyasaka, "Four-dimensional treatment planning and fluoroscopic real-time tumor tracking radiotherapy for moving tumor," *Int. J. Radiat. Oncol., Biol., Phys.* **48**(2), 435–442 (2000).
  - <sup>25</sup>H. Shirato, S. Shimizu, T. Kunieda, K. Kitamura, M. van Herk, K. Kagei, T. Nishioka, S. Hashimoto, K. Fujita, H. Aoyama, K. Tsuchiya, K. Kudo, and K. Miyasaka, "Physical aspects of a real-time tumor-tracking system for gated radiotherapy," *Int. J. Radiat. Oncol., Biol., Phys.* **48**(4), 1187–1195 (2000).
  - <sup>26</sup>B. Cho, P. R. Poulsen, A. Sloutsky, A. Sawant, and P. J. Keall, "First demonstration of combined kV/MV image-guided real-time dynamic multileaf-collimator target tracking," *Int. J. Radiat. Oncol., Biol., Phys.* **74**(3), 859–867 (2009).
  - <sup>27</sup>W. Liu, R. D. Wiersma, W. Mao, G. Luxton, and L. Xing, "Real-time 3D internal marker tracking during arc radiotherapy by the use of combined MV-kV imaging," *Phys. Med. Biol.* **53**(24), 7197–7213 (2008).
  - <sup>28</sup>R. D. Wiersma, W. Mao, and L. Xing, "Combined kV and MV imaging for real-time tracking of implanted fiducial markers," *Med. Phys.* **35**(4), 1191–1198 (2008).
  - <sup>29</sup>J. C. Park, S. H. Park, J. H. Kim, S. M. Yoon, S. S. Kim, J. S. Kim, Z. Liu, W. T. Watkins, and W. Y. Song, "Four-dimensional cone-beam computed tomography and digital tomosynthesis reconstructions using respiratory signals extracted from transcutaneously inserted metal markers for liver SBRT," *Med. Phys.* **38**(2), 1028–1036 (2011).
  - <sup>30</sup>N. Becker, W. L. Smith, S. Quirk, and I. Kay, "Using cone-beam CT projection images to estimate the average and complete trajectory of a fiducial marker moving with respiration," *Phys. Med. Biol.* **55**(24), 7439–7452 (2010).
  - <sup>31</sup>T. E. Marchant, A. M. Amer, and C. J. Moore, "Measurement of inter and intra fraction organ motion in radiotherapy using cone beam CT projection images," *Phys. Med. Biol.* **53**(4), 1087–1098 (2008).
  - <sup>32</sup>P. R. Poulsen, B. Cho, and P. J. Keall, "A method to estimate mean position, motion magnitude, motion correlation, and trajectory of a tumor from cone-beam CT projections for image-guided radiotherapy," *Int. J. Radiat. Oncol., Biol., Phys.* **72**(5), 1587–1596 (2008).
  - <sup>33</sup>I. Vergalaso, J. Maurer, and F. F. Yin, "Potential underestimation of the internal target volume (ITV) from free-breathing CBCT," *Med. Phys.* **38**(8), 4689–4699 (2011).